Final Report for AOARD Grant FA2386-09-1-4117

"Formation of Sphere-like Au Nanoparticles on Substrate with Laser Illumination and Their Surface Plasmon Behaviors"

September 17, 2010

Name of Principal Investigators: Chih-Chung (C. C.) Yang

- e-mail address : ccy@cc.ee.ntu.edu.tw
- Institution : Graduate Institute of Photonics and Optoelectronics, National Taiwan University
- Mailing Address : No. 1, Roosevelt Road, Section 4, Taipei, 10617 Taiwan
- Phone : 886-2-23657624
- Fax : 886-2-23652637

Period of Performance: 06/01/2009– 05/31/2010

Abstract: This research report includes two parts. First, the fabrications of sphere-like Au nanoparticles (NPs) of fixed orientation on sapphire, GaN, and SiO_2 substrates through the irradiation of a few pulses of 266-nm laser onto Au thin films deposited on the substrates are demonstrated. The top-view diameter, contact angle on substrate, surface population density, and surface coverage percentage of the NPs can be controlled by the Au thin film thickness, laser energy density, substrate choice, and the gas or liquid, in which the Au thin film is immersed during laser irradiation. Due to the fixed orientation of NPs, optical transmission measurements show clear in-plane and out-of-plane localized surface plasmon resonance (LSPR) features, including the air resonance feature dictated by the gas or liquid immersing the NPs during transmission measurement, the in-plane substrate resonance feature controlled by the substrate material and the contact angle, and the out-of-plane resonance feature, which is strongly influenced also by the substrate material and the contact angle. Numerical simulations based on the finite-element method using the experimental parameters show highly consistent LSPR spectral positions and their variation trends. From the simulation results, one can also observe the relative importance between NP absorption and scattering in contributing to the extinction. This simple laser-irradiation method for fabricating fixed-orientation sphere-like Au NPs of no aggregation and of strong adhesion to the substrate is useful for developing polarization-sensitive LSPR bio-sensing. In the second part, helical deposition of InGaN with a quasi-periodical indium content distribution along the growth direction for growing InGaN nanoneedles with the vapor-liquid-solid growth mode by using Au nanoparticles, which are formed on a GaN template with pulsed laser irradiation, as catalyst in a metalorganic chemical vapor deposition reactor is deduced. The deduction is based on the analyses of the scanning results in the high angle annular dark field and energy dispersive X-ray operations of transmission electron microscopy measurements. In such measurements, the composition variations along and perpendicular to the growth direction (the c-axis) are scanned. The alternating indium content along the growth direction is attributed to a pulsed behavior of indium super-saturation process in the catalytic Au droplet at the top of an InGaN nanoneedle. The helical deposition can be due to the formation of screw-type dislocations around the bases of InGaN nanoneedles for initiating spiral growth.

Report Documentation Page

Form Approved
OMB No. 0704-0188

1. REPORT DATE	2. REPORT TYPE	3. DATES COVERED
24 SEP 2010	**Final**	**29-04-2009 to 14-09-2010**

4. TITLE AND SUBTITLE
Formation of Sphere-like Au Nanoparticles on Substrate with Laser Illumination and Their Surface Plasmon Behaviors

5a. CONTRACT NUMBER
FA23860914117

5b. GRANT NUMBER

5c. PROGRAM ELEMENT NUMBER

6. AUTHOR(S)
Chih-Chung Yang

5d. PROJECT NUMBER

5e. TASK NUMBER

5f. WORK UNIT NUMBER

7. PERFORMING ORGANIZATION NAME(S) AND ADDRESS(ES)
Institute of Electro-Optical Engineering, Room 445,National Taiwan University,Taipei 10617,Taiwan,NA,NA

8. PERFORMING ORGANIZATION REPORT NUMBER
N/A

9. SPONSORING/MONITORING AGENCY NAME(S) AND ADDRESS(ES)
AOARD, UNIT 45002, APO, AP, 96337-5002

10. SPONSOR/MONITOR'S ACRONYM(S)
AOARD

11. SPONSOR/MONITOR'S REPORT NUMBER(S)
AOARD-094117

12. DISTRIBUTION/AVAILABILITY STATEMENT
Approved for public release; distribution unlimited

13. SUPPLEMENTARY NOTES

14. ABSTRACT
Fabrication of sphere-like Au nanoparticles (NPs) of fixed orientation on sapphire, GaN, and SiO2 substrates through the irradiation of a few pulses of 266-nm laser onto Au thin films deposited on the substrates was demonstrated. Numerical simulations based on the finite-element method using the experimental parameters show highly consistent localized surface plasmon resonance spectral positions and their variation trends. From the simulation results, one can also observe the relative importance between NP absorption and scattering in contributing to the extinction. This simple laser-irradiation method for fabricating fixed-orientation sphere-like Au NPs of no aggregation and of strong adhesion to the substrate is useful for developing polarization-sensitive LSPR bio-sensing. In addition, helical deposition of InGaN with a quasi-periodical indium content distribution along the growth direction for growing InGaN nanoneedles with the vapor-liquid-solid growth mode by using Au nanoparticles, which are formed on a GaN template with pulsed laser irradiation, as catalyst in a metalorganic chemical vapor deposition reactor is deduced.

15. SUBJECT TERMS
Semiconductor Materials, Electronics Device and Materials

16. SECURITY CLASSIFICATION OF:			17. LIMITATION OF ABSTRACT	18. NUMBER OF PAGES	19a. NAME OF RESPONSIBLE PERSON
a. REPORT	b. ABSTRACT	c. THIS PAGE			
unclassified	**unclassified**	**unclassified**	**Same as Report (SAR)**	**21**	

Part I: Fabrication of Fixed-orientation Sphere-like Au Nanoparticles on Substrate with Laser Irradiation and Their Polarized Localized Surface Plasmon Behaviors

1. Introduction

Metal nanoparticles (NPs) can find important applications in recently developed nanotechnologies, particularly in plasmonics for bio-sensing.[1-5] Localized surface plasmon (LSP) resonance (LSPR) features on metal NPs, which are prepared on a substrate, have been used for bio-sensing based on the resonance wavelength dependence on the refractive index of surrounding liquid. Such a measurement can lead to refractive index measurement sensitivity as high as 880 nm spectral shift per refractive index unit.[6] Among the methods of fabricating metal NPs, chemical synthesis is the most widely used approach.[7-9] Normally, in fabricating an LSPR device, chemically synthesized metal NPs, such as Au and Ag, are spin-coated on a transparent substrate. However, the bonding between the metal NPs and the used substrate in such a device is usually weak leading to unstable detection. Also, the NP aggregation can be a major problem in fabricating such a device. Besides spin-coating chemically synthesized metal NPs on a substrate, several methods have been developed for fabricating metal nanostructures on a substrate, such as the structures of nanoring, nanodisk, and nanoprism.[6,10-15] Among them, colloidal lithography[6,10] and nanosphere lithography[11] have been used for directly fabricating metal NPs on a substrate. Plasmonic nanolithography for forming metal nanodot arrays was also reported.[12] Because the size and shape of a metal NP determine the LSPR wavelengths, shaping a metal NP is an important issue. The shape of an NP can be manipulated through laser-induced LSPR excitation during the chemical synthesis process.[13-15] Also, the geometry of a metal NP can be modified by direct laser irradiation when the NP is in either liquid or gas environment.[16-18] Although various methods for preparing metal NPs on a substrate have been implemented, they either correspond to complicated processes or lead to random orientations of NPs on substrate. A fixed orientation of NPs on a substrate can result in polarization-sensitive LSPR excitation for more versatile sensing application. If a simple technique for directly fabricating metal NPs of fixed orientation and controllable parameters on a substrate with strong adhesion, the LSPR sensing technology can be significantly improved.

In this part of the report, we describe a simple method for fabricating substrate adhesive Au NPs of no aggregation based on a process of laser ablation and annealing. The size, shape, surface density, and coverage of Au NPs on a substrate can be controlled by laser energy density, substrate material and surface condition, deposited Au film thickness, and the liquid covering the Au film during laser irradiation. With optical transmission measurements, the in-plane and out-of-plane LSPR features can be clearly identified due to the fixed NP orientation on substrate. The spectral features of substrate-affected LSPR modes rely on the size, Au/substrate contact area, substrate material, and surrounding gas or liquid. Numerical simulations based on the finite-element method show highly consistent results in the LSPR-induced extinction spectral features. The used laser came from the fourth-harmonic generation (266 nm) of a Q-switched Nd:YAG laser of adjustable pulse repetition rate. In Au NP fabrication, one or a few laser pulses were applied onto an Au thin film, which was deposited on a double-side-polished substrate with electron-beam evaporation. The used substrates are transparent in the visible range for transmission measurements with a white light source.

2. Experimental Results

The four parts of Fig. 1 show the results of laser irradiation with two pulses onto a 10-nm Au thin film on a sapphire substrate. The laser pulse energy density was around 30 mJ/cm^2. Figures 1(a) and 1(b) show the plan-view scanning electron microscopy (SEM) images of the surfaces before and after laser irradiation, respectively. One can see the cracks of the Au thin film on sapphire substrate in Fig. 1(a). After laser irradiation, sphere-like Au NPs of various sizes can be observed in Fig. 1(b). Figure 1(c) shows a tilted SEM image of the Au NPs. One can observe the cut-facet of the sphere-like NPs. To understand the NP size distribution, we developed a computer program to evaluate the sizes and population density of those NPs based on the plan-view SEM image. The NP diameter distribution is shown in Fig. 1(d). Here, the NP diameter shows a nearly normal distribution ranging from 30 through 170 nm with the average diameter around 85 nm. The contact angle, θ_c, between an Au NP and the substrate is defined as that between the contact facet and the tangential of the Au body at one of the contact edges, as demonstrated in the insert of Fig. 1(d). During the laser irradiation process, the gold film is melted due to the absorption of UV laser. The contact angle of an Au NP in solid phase is close to that of a liquid Au droplet at a temperature close to the melting point. Therefore, this contact angle can be ideally evaluated by using the Young-Dupré formula as[19]

$$\gamma_{SV} - \gamma_{SL} - \gamma_{LV} \cos\theta_c = 0 \quad (1)$$

Here, γ_{LV}, γ_{SV}, and γ_{SL} are the surface tensions at the liquid/vapor (Au/air), solid/vapor (substrate/air), and solid/liquid (substrate/Au) interfaces, respectively. Note that a larger contact angle corresponds to an Au NP shape closer to a perfect sphere. The size of the contact angle or contact area depends on the material type of the substrate and the metal melting temperature. Based on the reaction-free theory, the contact angle of an Au sphere-like NP on sapphire is between 135 and 140 degrees.[20] Although it is difficult to accurately read the contact angle from the SEM image in Fig. 1(c), the estimated angle is close to the theoretical value.

Figures 2(a) and 2(b) show the similar results to those in Figs. 1(b) and 1(c), respectively, by using a GaN template as the substrate. The GaN template of 2 μm in thickness was grown on sapphire substrate with metalorganic chemical vapor deposition along the c axis at 1000 ^{o}C. Its surface roughness is below 0.5 nm. Under laser irradiation of five pulses at around 20 mJ/cm^2 in energy density onto a 7.5-nm thick Au film, sphere-like Au NPs are formed on GaN as shown in the plan-view and tilted SEM images of Figs. 2(a) and 2(b), respectively. The top-view diameter is distributed between 40 and 120 nm with the average value around 75 nm. From Fig. 2(b), the contact angle is estimated to be smaller than that on sapphire and should be smaller than 130 degrees. Au NPs were also fabricated on a SiO_2 template, which was obtained by depositing a 30-nm SiO_2 layer on a GaN template with plasma-enhanced chemical vapor deposition. A tilted SEM image of such NPs is shown in Fig. 2(c). Here, one can see a few relatively larger NPs, which have a contact angle close to 180 degrees. The details of laser irradiation conditions and resultant NP parameters are listed in Table I. The major function of laser irradiation is supposed to be thermal annealing. However, such a thermal annealing process is different from that based on furnace heating. In Fig. 2(d), we show a plan-view SEM image of Au nanostructures fabricated with a furnace-based process at 800 ^{o}C for 30 min from a 7.5-nm Au film on a GaN template. Here, the formed Au nanostructures are quite random in morphology, very much different from the sphere-like shape shown in Fig. 2(a). Therefore, laser irradiation leads to certain mechanisms besides heating.

Figure 3 shows the transmission spectra of the samples of Au NPs on sapphire and SiO_2 with the s (Sapphire-s and SiO_2-s) and p (Sapphire-p and SiO_2-p) incident polarization conditions when the incident angle is 60 degrees with respect to the normal of the substrate surface. With such an incident angle, in the case of s-polarized excitation, only the in-plane LSPR features can be excited. On the other hand, in the case of p-polarized excitation, both the in-plane and out-of-plane LSPR features are excited. As shown in Fig. 3, in the transmission spectrum of s-polarized excitation of the sapphire-based sample, two clear dip features can be identified, with one around 515 nm and the other around 565 nm. The feature around 565 nm is due to in-plane electron oscillation, which is affected by the contact facet of the Au NPs on the substrate, and is named as the in-plane substrate resonance (IPSR) feature. That around 515 nm corresponds to the LSPR of an Au NP completely surrounded by air and is named as the air resonance (AR) feature. This feature is red-shifted when the NPs are immersed in certain liquid during transmission measurement. In the transmission spectrum of the "Sapphire-p" case, a broad dip with the minimum around 545 nm can be observed. This broad dip is supposed to consist of three features, including the aforementioned AR and IPSR, and an out-of-plane resonance (OPR) feature around 545 nm. Similar in-plane and out-of-plane LSPR features have been observed in a periodic metal nanodisk structure.[21] This OPR LSP feature is also affected by the contact facet of an Au NP and the substrate material. In Fig. 3, the transmission behaviors of NPs on SiO_2 are quite different from those on sapphire. Because the contact angle of the NPs on SiO_2 is close to 180 degrees, the IPSR and OPR features are unclear. Only the AR feature is observed in either s- or p-polarized excitation. The significant contact between NPs and substrate is crucial for the generations of the IPSR and OPR features. The oscillating transmission behaviors in the SiO_2 sample are due to the Fabry-Perot effect between the air/SiO_2, SiO_2/GaN, and GaN/sapphire interfaces. To guide eyes, low-pass-filtering fitting curves are drawn on the oscillating transmission curves.

Figure 4 shows the transmission spectra of the Au-nanostructure samples on the GaN template with the curves of GaN-s and GaN-p for s- and p-polarized excitations, respectively. Here, the data of both samples fabricated by laser treatment and furnace-based thermal annealing are demonstrated. In all the curves here, Fabry-Perot oscillations can be clearly seen. Again, low-pass-filtering fitting curves are drawn to guide eyes. Here, in the sample of laser treatment, the AR feature merges into the dominating IPSR feature and cannot be clearly identified. The IPSR and OPR features are located around 655 and 533 nm, respectively. The relatively smaller contact angle and larger refractive index (~2.5) of GaN substrate leads to a larger spectral separation between the IPSR and OPR features, when compared with the case of sapphire substrate. The transmission behaviors of the sample

fabricated with furnace-based thermal annealing are quite different from those fabricated with laser treatment. In the thermal annealing case, although a broad-range IPSR feature can be identified, no feature corresponding to OPR or AR can be seen.

3. Numerical Studies

To confirm the LSPR features described above, we performed numerical simulation of plane wave incidence upon the structure of an Au NP on the substrate with the finite-element method (COMSOL) to evaluate the absorption (metal dissipation) and scattering spectra of the NP/substrate system. Then, the extinction spectra can be obtained by taking the summation of absorption and scattering. It is noted that the resonance peaks of absorption and scattering are not necessarily at the same spectral positions.[22] The six curves in Fig. 5(a) labeled by A-s, S-s, and E-s (A-p, S-p, and E-p) correspond to the absorption, scattering, and extinction spectra of NPs on sapphire when the incident wave is s- (p-) polarized with the incident angle at 60 degrees. The top-view NP diameter and the contact angle are assumed to be 85 nm and 135 degrees, respectively. The dielectric characteristics of Au can be found in literature.[23] In the E-s curve, one can see a peak around 570 nm and a shoulder on the high-energy side. The peak around 570 nm corresponds to the IPSR feature of the experimental data shown in Fig. 3. The shoulder originates from the AR feature around 515 nm. On the other hand, the broad hump of curve E-p consists of the contributions of IPSR, AR, and the OPR feature around 550 nm. The general agreements of the LSPR features between the experimental data and numerical simulations assure the correctness of data interpretation. In particular, as shown in Figs. 5(b)-5(d) for the field intensity distributions at 515 and 570 nm of the s-polarized excitation case, and at 550 nm of the p-polarized excitation case, the physical meanings of the AR, IPSR, and OPR features become clearer. The slight differences in spectral peak between the simulation and experimental results can be due to the imprecise assignments of NP parameters for simulation. It is noted that the intensity distribution in Fig. 5(d) contains the contributions of the AR, IPSR, and OPR features. As shown in Fig. 5(c) for the IPSR feature, the LSP field is mainly distributed near the two edges of the NP/substrate contact facet. This feature describes the in-plane electron oscillation on the Au NP near the substrate such that its characteristics are strongly influenced by the substrate material (refractive index) and the contact angle. On the other hand, as shown in Fig. 5(b), the AR feature describes a more uniform energy distribution on the two sides of the NP in the in-plane dimension. This feature is supposed to be influenced only by the NP size and the surrounding medium above the substrate. Then, in Fig. 5(d), one can clearly see more energy distributions at the top and bottom of the NP corresponding to the contribution of the OPR feature. In Fig. 5(a), one can also observe the relative importance of the absorption and scattering contributions to the three LSPR features. The AR feature is mainly caused by the absorption of Au NP. The scattering contribution to the IPSR feature becomes relatively more important even though it is still dominated by absorption. As to the OPR feature, the absorption and scattering contributions become comparable.

To further understand the effects of the refractive-index contrast between the substrate and the surrounding medium, and those of the imperfect sphere shape of the NP on the LSP spectral features, we performed the simulations under the conditions of an Au NP completely surrounded by air and by a medium of sapphire refractive index to give the spectral curves in Figs. 6(a) and 6(b), respectively. The NP diameter and the contact angle are still assumed to be 85 nm and 135 degrees, respectively. The label notations in Figs. 6(a) and (b) are the same as those in Fig. 5 for both s- and p-polarized excitations. Also, in either Fig. 6(a) or 6(b), the simulation results under the condition of perfect Au sphere, labeled by A-sphere, S-sphere, and E-sphere for absorption, scattering, and extinction, respectively, are demonstrated. Here, one can see that when the NP is completely surrounded by air, the extinction is dominated by the contribution of absorption, whose resonance feature is slightly blue shifted from that of the scattering contribution. Also, the spectral position of the unique LSPR feature (AR) around 515 nm is not significantly affected by the NP orientation, i.e., excitation polarization. A small blue shift of the LSPR feature in p-polarized excitation by ~5 nm from that in s-polarized excitation is observed. Meanwhile, with perfect sphere shape, the extinction resonance feature is located at almost the same spectral position as those of the s- and p-polarized LSPR of an imperfect sphere. However, as shown in Fig. 6(b), when an NP is completely surrounded by a medium of 1.76 in refractive index, scattering feature around 650 nm dominates the contribution to extinction. The spectral peak positions of E-s, E-sphere, and E-p curves are located at 650, 640, and 635 nm, respectively. In other words, the imperfect sphere geometry and the excitation orientation are important factors in determining the LSPR features when the surrounding refractive index is larger than unity. From Fig. 6, one can realize the importance of the NP contact angle and substrate material

in controlling the LSPR spectral position. It is noted that a second LSPR feature exists around 560 nm leading to the kinks on the high-energy side of the extinction curves.

Figure 7 shows the simulation results of the Au NP sample on GaN by assuming that the NP diameter is 75 nm and the contact angle is 125 degrees. In the extinction spectrum of s-polarized excitation, the features of IPSR around 640 nm and AR around 515 nm can be clearly identified. Then, in the extinction spectrum of p-polarized excitation, the dominating feature of OPR around 545 nm can be observed besides the IPSR and AR (as the shoulder) features. In this sample with GaN as the substrate, although the major contribution to the AR extinction is absorption, the contributions of absorption and scattering to the IPSR and OPR extinctions are comparable. The simulation results in Fig. 7 are highly consistent with the experimental data in Fig. 4.

As mentioned earlier, the Au NP size and contact angle can be slightly controlled by the laser pulse energy, Au film thickness, and substrate selection. The Au NP parameters can also be controlled by the covering liquid on the Au thin film during laser irradiation. In Table I, we list the parameters of Au NPs fabricated under the conditions of air, water, and methanol coverage during laser irradiation. The results of the air coverage condition have been discussed earlier related to Fig. 1. For comparison, the results of the NPs on GaN and SiO_2 discussed earlier are also summarized in Table I. Among the three samples of sapphire substrate fabricated under the conditions of air, water, and methanol coverage of Au thin film during laser irradiation, one can see the changes of NP average size, contact angle, NP density, and surface coverage. Although it is difficult to exactly determine the contact angles under the conditions of water and methanol coverage during laser irradiation, they are surely significantly larger than that under the fabrication condition of air coverage. Generally speaking, under the fabrication condition of methanol coverage, the NP size is the largest, the NP density is the smallest, and the surface coverage is the smallest, all followed by the condition of water coverage, among the three samples of sapphire substrate. In Fig. 8, we show the transmission spectra of the three samples with s- and p-polarized excitations. In the curves of s-polarized excitation, one can see the slight blue shift of the IPSR feature and the relatively more important contribution of the AR feature when water and methanol are applied during laser irradiation. On the other hand, the broad dip (containing the AR, IPSR, and OPR features) under p-polarized excitation is red shifted when water or methanol is used, indicating that the OPR feature is red shifted. In Figs. 9(a) and 9(b), the simulated absorption, scattering and extinction spectra under the conditions of air, water, and methanol coverage with s- and p-polarized excitations, respectively, are shown. The NP parameters for simulations, including NP diameters and contact angles, are shown in Table I. Here, one can see the slight blue shift trend (570 to 565 nm) of the IPSR feature and the slight red shift trend (550 to 565 nm) of the OPR feature when air coverage is replaced by water and then by methanol coverage. Such trends are consistent with the experimental observations shown in Fig. 8. It is noted that the relative extinction levels among the three samples shown in Figs. 9(a) and 9(b) are not consistent with the relative dip levels shown in Fig. 8. Such an inconsistency is attributed to the different NP densities among the three samples. As shown in Table I, the sample of air (methanol) coverage has the highest (lowest) NP density that may reverse the variation trend of the total extinction. However, it is believed that other factors should be included for explaining the variation trend of extinction, including the possible variation in measurement condition and the LSP coupling between the neighboring NPs. Because of the random distribution nature of NPs, some of NPs are close enough to generate LSP coupling. Such coupling behaviors are expected to shift the LSPR spectral position and statistically result in a broadened LSPR spectral feature.

4. Summary

In summary, we have demonstrated the fabrication of sphere-like Au NPs of fixed orientation on sapphire, GaN, and SiO_2 substrates by the irradiation of a few UV laser pulses onto Au thin films, which were deposited on the substrates. The top-view diameter, contact angle on substrate, surface density and coverage of the NP could be controlled by Au thin film thickness, laser energy density, substrate choice, and the gas or liquid covering the Au thin film during laser irradiation. White light transmission measurements showed clear in-plane and out-of-plane LSPR features, including the AR feature dictated by the surrounding gas or liquid immersing the NPs during transmission measurement, the IPSR feature controlled by the substrate material and the contact angle, and the OPR feature, which was strongly influenced also by the substrate material and the contact angle. Numerical simulations based on the finite-element method using the experimental parameters showed highly consistent LSPR spectral positions and their variation trends. From the simulation results, one could also see the relative importance between NP absorption and scattering in contributing to the total

extinction.

References

(1) Elghanian, R.; Storhoff, J. J.; Mucic, R. C.; Letsinger, R. L.; Mirkin, C. A. *Science* **1997**, *277*, 1078.
(2) Haes, A. J.; Van Duyne, R. P. *J. Am. Chem. Soc.* **2002**, *124*, 10596-10604.
(3) Haes, A. J.; Hall, W. P.; Chang, L.; Klein, W. L.; Van Duyne, R. P. *Nano Lett.* **2004**, *4*, 1029-1034.
(4) Chithrani, B. D.; Ghazani, A. A.; Chan, W. C. W. *Nano Lett.* **2006**, *6*, 662-668.
(5) Chen, Y.; Munechika, K.; Ginger, D. *Nano Lett.* **2007**, *7*, 690–696.
(6) Larsson, E. M.; Alegret, J.; Käll, M.; Sutherland, D. S. *Nano Lett.* **2007**, *7*, 1256-1263.
(7) Anker, J. N.; Hall, W. P.; Lyandres, O.; Shah, N. C.; Zhao, J.; Van Duyne, R. P. *Nat. Mater.* **2008**, *7*, 442–453.
(8) Yu, Y. Y.; Chang, S. S.; Lee, C. L.; Wang, C. R. C. *J. Phys. Chem. B* **1997**, *101*, 6661-6664.
(9) Jin, R.; Cao, Y.; Mirkin, C. A.; Kelly, K. L.; Schatz, G. C.; Zheng, J. G. *Science* **2001**, *294*, 1901-1903.
(10) Aizpurua, J.; Hanarp, P.; Sutherland, D. S.; Kall, M.; Bryant, G. W.; de Abajo, F. J. G. *Phys. Rev. Lett.* **2003**, *90*, 057401.
(11) Haynes, C. L.; Van Duyne, R. P. *J. Phys. Chem. B* **2001**, *105*, 5599- 5611.
(12) Srituravanich, W.; Fang, N.; Sun, C.; Luo, Q.; Zhang, X. *Nano Lett.* **2004**, *4*, 1085-1088.
(13) Maillard, M.; Huang, P.; Brus, L. *Nano Lett.* **2003**, *3*, 1611-1615.
(14) Jin, R.; Cao, Y. C.; Hao, E.; Metraux, G. S.; Schatz, G. C.; Mirkin, C. A. *Nature* **2003**, *425*, 487-490.
(15) Sherry, L. J.; Jin, R. C.; Mirkin, C. A.; Schatz, G. C.; Van Duyne, R. P. *Nano Lett.* **2006**, *6*, 2060-2065
(16) Simakin, A. V.; Voronov, V. V.; Shafeev, G. A.; Brayner, R.; Bozon-Verduraz, F. *Chem. Phys. Lett.* **2001**, *348*, 182-186.
(17) Habenicht, A; Olapinski, M.; Burmeister, F.; Leiderer, P.; Boneberg, J. *Science* **2005**, *309*, 2043-2045.
(18) Huang, W.; Qian, W.; El-Sayed, M. A. *J. Appl. Phys.* **2005**, *98*, 114301.
(19) Sangiorgi, R; Muolo, M. L.; Chatain, D; Eustathopoulos, N *J. Am. Ceram. Soc.* **1988**, *71*, 742-748.
(20) Didier, F; Jupille, J *Surf. Sci.* **1994**, *314*, 378-384.
(21) Hägglund, C.; Zäch, M.; Petersson, G; Kasemo, B. *Appl. Phys. Lett.* **2008**, *92*, 053110.
(22) Jain, P. K.; Lee, K. S.; El Sayed, I. H.; El Sayed, M. A. *J. Phys. Chem. B* **2006**, *110*, 7238-7248.
(23) *Handbook of Optical Constants of Solids*, Academic Press, Boston, **1991**.

Table I. Various Au NP parameters under various fabrication conditions.

substrate	sapphire	sapphire	sapphire	GaN	SiO_2
Au thickness (nm)	10	10	10	7.5	10
Laser energy density (mJ/cm^2)	30	30	30	20	20
Number of pulses	2	2	2	5	1
Covering gas/liquid	air	water	methanol	air	air
Average NP diameter (nm)	85	97	99	75	38
Estimated contact angle (degree)	135	~145	~145	<130	~180
NP density (cm^{-2})	1.75×10^9	1.25×10^9	1.02×10^9	2.78×10^9	1.29×10^{10}
Surface coverage (%)	13.18	12.8	10.6	14.04	17.7

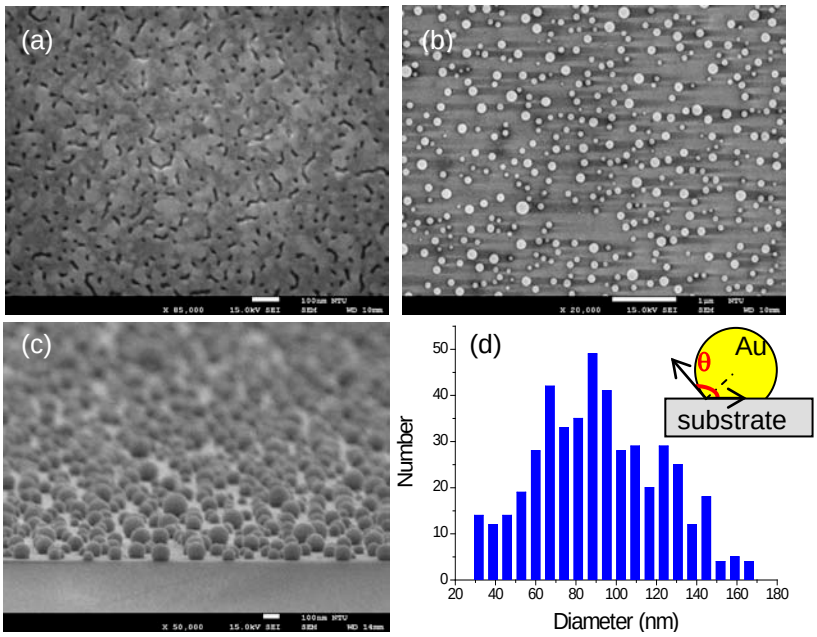

Figure 1 (a) Plan-view SEM images of the Au thin film (10 nm in thickness) on sapphire substrate before laser irradiation; (b) Plan-view SEM image of the NPs after laser irradiation; (c) Tilted SEM image after laser irradiation; (d) Top-view diameter distribution of the NPs formed on sapphire substrate. The insert of part (d) shows the definition of the contact angle.

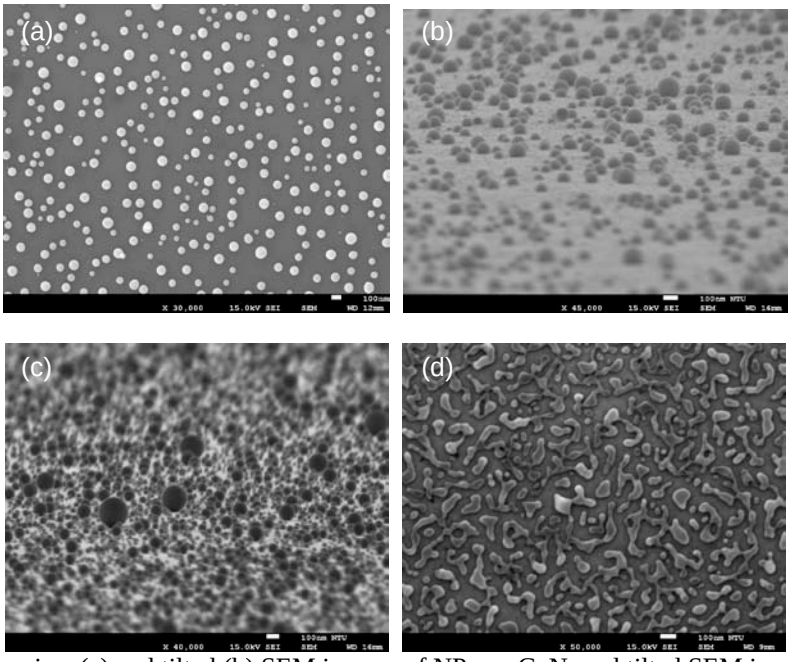

Figure 2 Plan-view (a) and tilted (b) SEM images of NPs on GaN, and tilted SEM image of NPs on SiO_2 (c). In part (d), a plan-view SEM image of the Au nanostructures after furnace-based thermal annealing at 800^{o}C for 30 min is demonstrated.

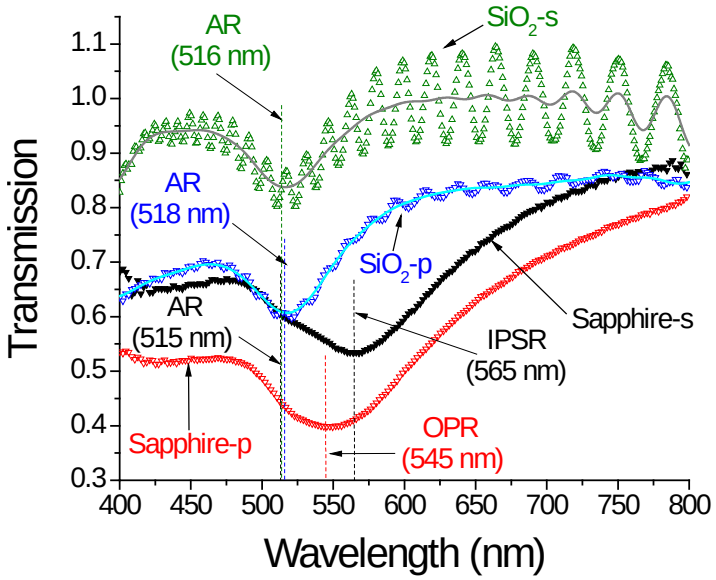

Figure 3 Transmission spectra of the Au NPs on sapphire and SiO_2 under the s- (Sapphire-s and SiO_2-s) and p-polarized (Sapphire-p and SiO_2-p) excitation conditions when the incident angle is 60 degrees with respect to the normal direction.

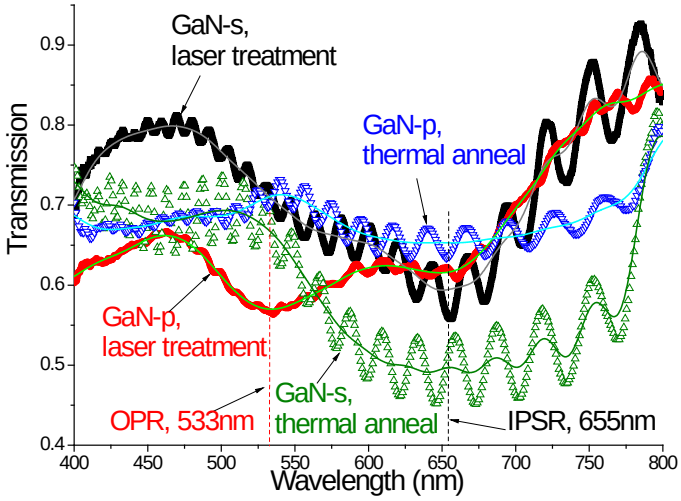

Figure 4 Transmission spectra of the Au NPs on GaN under the s- (GaN-s, laser treatment) and p-polarized (GaN-p, laser treatment) excitation conditions when the incident angle is 60 degrees with respect to the normal direction. For comparison, the transmission spectra of the Au nanostructures on GaN fabricated by furnace-based thermal annealing are also shown (GaN-s, thermal anneal and GaN-p, thermal anneal).

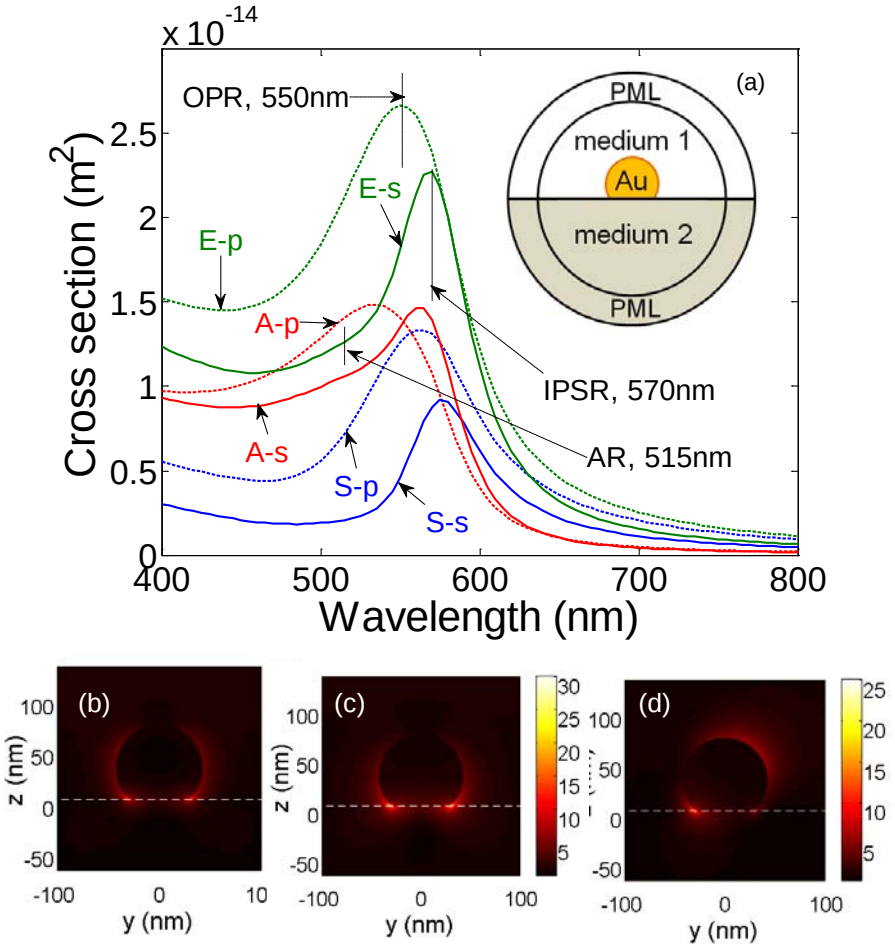

Figure 5 (a) Simulated absorption (A-), scattering (S-), and extinction (E-) spectra of the s- and p-polarized excitation with the incident angle at 60 degrees; (b) and (c): Field intensity distributions under s-polarized excitation at 515 and 570 nm, corresponding to the AR and IPSR features, respectively; (d): Field intensity distribution under p-polarized excitation at 550 nm, corresponding to the combinations of the OPR, AR, and IPSR features.

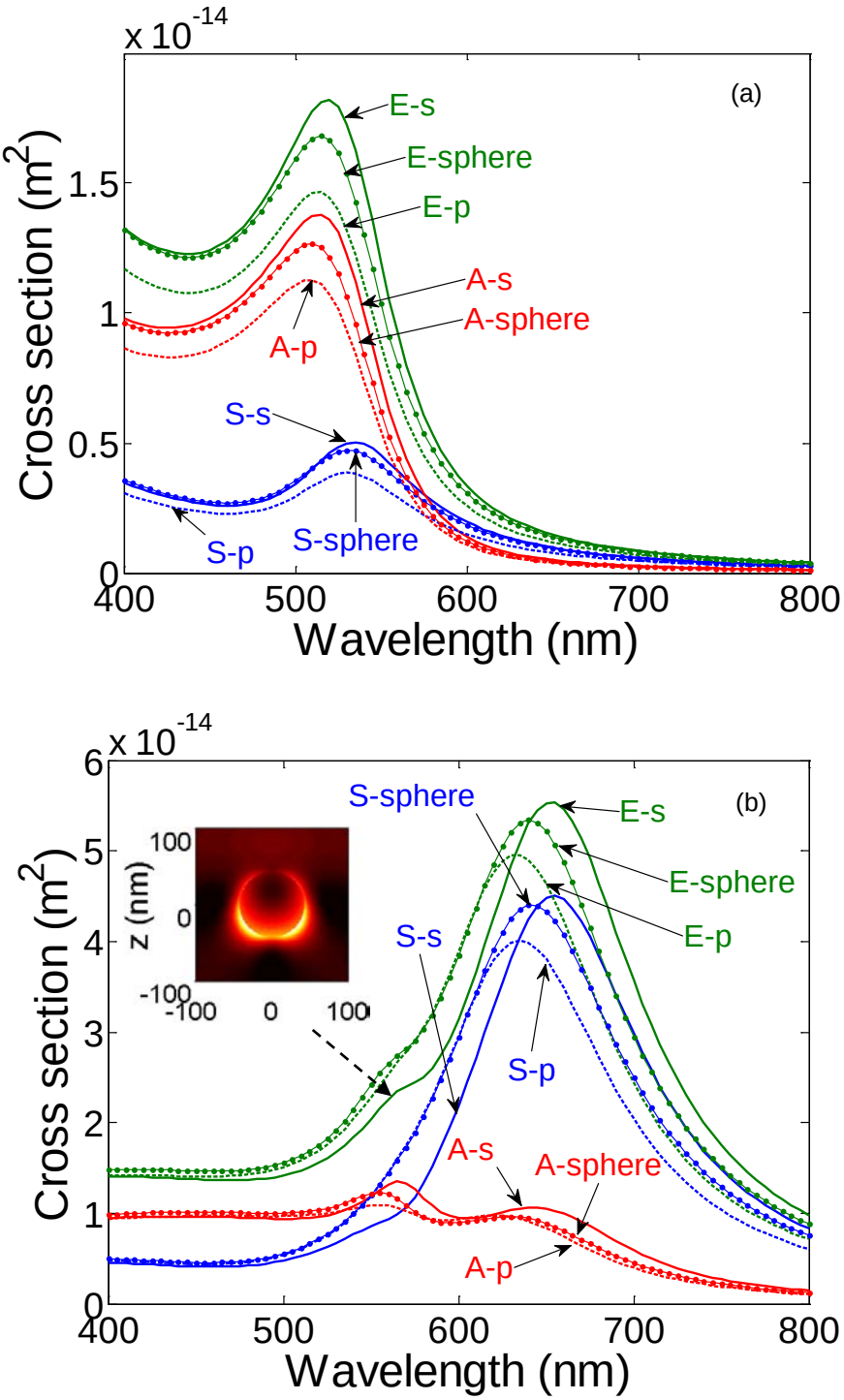

Figure 6 Simulated absorption, scattering, and extinction spectra of an Au NP with the parameters given for the results in Fig. 5 but completely surrounded by the media of air (a) and sapphire (b) refractive indices. The results of a perfectly spherical NP as labeled by "-sphere" are also shown in either part (a) or (b) for comparison.

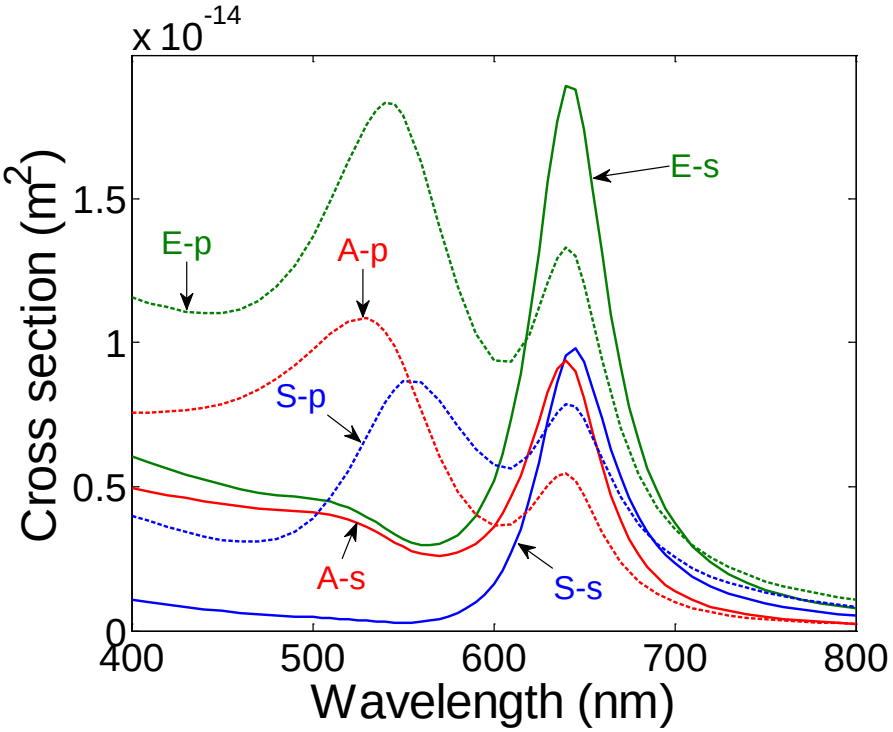

Figure 7 Simulated absorption, scattering, and extinction spectra of an Au NP on GaN with the s- and p-polarized excitations.

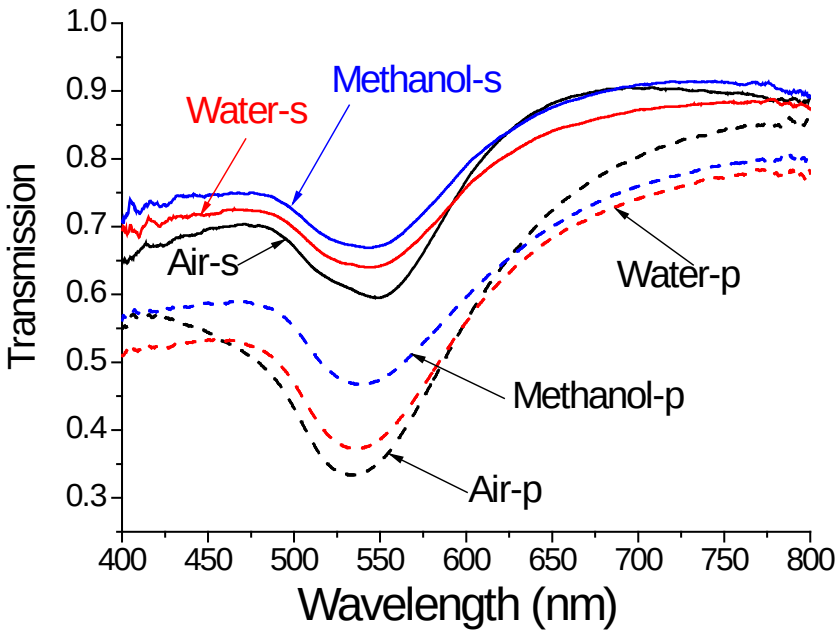

Figure 8 Transmission spectra of the samples of Au NPs on sapphire fabricated with air, water, and methanol coverage on Au thin films during laser irradiation under the s- and p-polarized excitations.

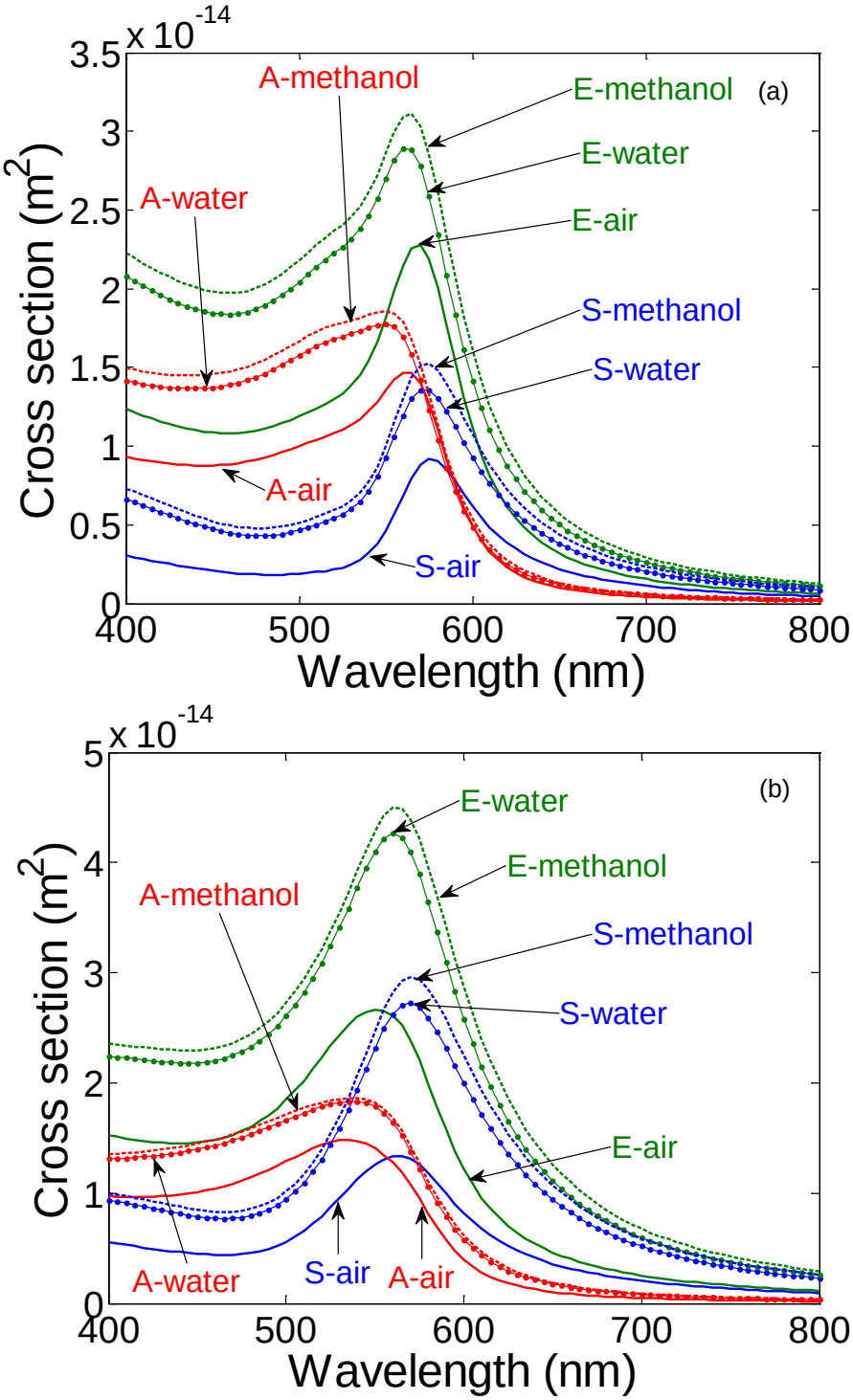

Figure 9 Simulated absorption, scattering, and extinction spectra of the Au NPs fabricated with air, water, and methanol coverage on Au thin films during laser irradiation under the s- (a) and p-polarized (b) excitations.

Part II: Spiral Deposition with Alternating Indium Composition in Growing an InGaN Nano-needle with the Vapor-liquid-solid Growth Mode

1. Introduction

Quasi-one dimensional (1-D) semiconductor structures have attracted much attention for many novel applications. Such a structure has the advantages of low dislocation density, lateral strain relaxation, and possibly quantum confinement. For wide-band gap nitrides, although the growth of GaN nanocolumns, nanoposts, nanorods, and nanowires have been widely demonstrated [1-6], the growth of quasi-1-D InGaN structures, which have application potential in fabricating high-efficiency solar cells and light-emitting devices, is rarely reported [7,8], particularly those grown with metalorganic chemical vapor deposition (MOCVD). Among various growth techniques, the vapor-liquid-solid (VLS) growth mode has been widely used for growing quasi-1-D structures [9-13]. In this growth mode, either self-metal or extrinsic-metal catalyst is needed for transferring vapor elements into crystalline structure through the molten catalyst metal droplet. In other words, the molten metal absorbs composition elements to reach a super-saturation condition, under which the composition elements are precipitated on the seeding semiconductor beneath the catalyst metal droplet. With this approach, quasi-1-D semiconductor structures can be formed following the trace of the catalyst metal droplet.

In this part of the report, the spiral deposition behaviors of InGaN with alternating indium composition in growing InGaN nanoneedles (NNs) with the VLS mode are reported. Au nanoparticles (NPs) formed with laser irradiation onto an Au thin film on a GaN template [14] are used as catalyst in such an MOCVD growth. From the transmission electron microscopy (TEM) measurements, including high angle annular dark field (HAADF) and energy dispersive X-ray (EDX) operations, we observe the alternating "anti-symmetric" indium content distribution with respect to an almost vertical axis along the c-direction near the center of an InGaN NN. Also, along the growth direction, indium content varies quasi-periodically. It is deduced that the VSL growth follows a helical deposition pattern of InGaN with a quasi-periodical indium composition variation in an nm scale.

2. InGaN Nanoneedle Growth and Characterization Methods

The sphere-like Au NPs for serving as the catalyst were prepared on a 2-μm GaN template, which was grown at 1000 ^{o}C on c-plane sapphire substrate with MOCVD, by first depositing an Au thin film of 7.5 nm in thickness and then irradiating the Au thin film with the fourth-harmonic of a Q-switched Nd:YAG laser. After the irradiation of five laser pulses of 20 mJ/cm^2 in energy density, sphere-like Au NPs of 75 nm in average diameter and 2.78×10^9 cm^{-2} in surface particle density were formed. A plan-view scanning electron microscopy (SEM) image of the Au NPs on GaN is shown in Fig. 1. The GaN template with Au NPs was used for GaN and InGaN overgrowth in an MOCVD reactor. Figure 2 shows a cross-section SEM image of GaN overgrowth at 700 ^{o}C for 30 min. Here, one can see that the Au NPs are embedded in GaN and no quasi-1-D nanostructure is formed. In other words, Ga atoms are not effectively absorbed by molten Au NPs for VLS growth. It is noted that the Au NPs are expected to be melting at the temperature of 700 ^{o}C even though it is significantly lower than the meting point of bulk Au at 1064 ^{o}C. The molten Au droplets on the template are in sphere-like shapes due to surface tension.

Then, InGaN growth was performed on another GaN template with the similar Au NPs also at 700 ^{o}C for 60 min after GaN growth at 600 ^{o}C for 10 min. The first-stage GaN growth is needed for filling up the spacing between Au NPs before InGaN growth; otherwise, no quasi-1-D InGaN structure can be fabricated. Figure 3 shows a tilted SEM image of the grown InGaN NNs. At the tips of some InGaN NNs, the residual Au NPs (dark spots) can still be seen. The bases of some of those NNs are larger than 100 nm in size, which is larger than the sizes of the formed Au NPs. It was observed that neighboring Au NPs on a GaN template could be combined to form a larger molten Au droplet for serving as catalyst. Au atoms might be mixed into precipitated InGaN during the catalytic growth such that an Au droplet becomes smaller and the InGaN cross section also becomes smaller along the growth in the c-direction to form the needle geometry.

Figure 4 demonstrates a cross-section TEM HAADF image showing three InGaN NNs with the residual Au NPs removed (to show the flat tops). A Philips Tecnai F20 G2 FEI-TEM system was used for HAADX and EDX observations with the electron beam size of 1 nm. Also, a Bede 1 high-resolution X-ray diffraction (XRD) facility was used for XRD evaluation of the InGaN NN sample. From the result of reciprocal space mapping (RSM), as shown in Fig. 5, the InGaN is fully-strain relaxed. Here, the vertical and slant dashed lines correspond to the fully-strained and

fully-strain-relaxed conditions, respectively. Figure 6 shows the XRD ω-2θ-scan intensity distribution of the InGaN NN sample. The InGaN peak here corresponds to an average indium content of 22 %.

3. Analyses of Transmission Electron Microscopy Images

igure 7 shows the HAADF close-up image of an InGaN NN. The circular bright spots in the background represent the residual Au NPs. In the NN, one can clearly observe an almost vertical axis around the center of the NN (indicated by the two arrows in the NN region). Also, the bright and dark contrast distribution shows a quasi-periodical pattern along the vertical direction (the c-axis) and a roughly "anti-symmetric" pattern along the horizontal direction with respect to the aforementioned vertical axis. In other words, if the contrast is brighter on the right-hand side at a certain height of the NN, it becomes darker on the same side in the next half-cycle of the quasi-period when moving along the vertical axis. It is noted that in a HAADF image, a brighter region corresponds to higher indium content. Therefore, it is deduced that the InGaN growth follows a helical deposition pattern with a quasi-periodical indium content distribution along the growth direction [15-20].

To prove this deduction, vertical and horizontal EDX signal and HAADF intensity distributions along the roughly marked vertical and horizontal dashed lines in Fig. 7 (red and blue dashed lines for EDX and HAADF, respectively) are analyzed. Figure 8 shows the horizontal EDX (the left ordinate for indium atomic %) and HAADF (the right ordinate) data distributions along the horizontal dashed lines (at different heights) in Fig. 7. The spatial resolution of EDX scanning is around 1 nm. That of HAADF is expected to be higher. In Fig. 8, one can see the two generally different levels in either indium atomic % of EDX or HAADF intensity between the positive and negative coordinates. It is noted that the zero points of the horizontal distance are roughly assigned to show the "anti-symmetric" patterns. Around the vertical axis (at 0 distance here), either HAADF intensity or EDX indium atomic % shows a local maximum.

Figure 9 shows the results of HAADF and EDX scanning, similar to Fig. 8, along the vertical direction. The generally decreasing trend of HAADF intensity along the c-axis can be caused by imperfect imaging operation and cannot be interpreted as a decreasing trend of indium content. To see the nm-scale indium composition variation along the c-axis, we performed Fourier transforms of the spatial signal variations in Fig. 9 to give the normalized spatial-frequency spectra in Fig. 10. In this figure, although one cannot observe any dominating spatial-frequency component within the concerned range (>0.1 nm^{-1}) in either HAADF or EDX scanning result, a few consistent peaks between the HAADF and EDX scanning results can be identified, including those at 0.22 and 0.3 nm^{-1}. These two spatial-frequency features correspond to 4.55 and 3.33 nm in period in a quasi-periodical variation of indium content. They may represent the two major components of indium content variation.

4. Discussions

Based on the "anti-symmetric" HAADF and EDX data distributions with respect to the vertical axis, one can imagine a mechanism of helical deposition of InGaN atoms with alternating indium composition of a high and a low level. Because a TEM image shows the integration of atomic distribution along the electron beam direction, the projection of such an integration of a helical indium distribution can lead to the alternating HAADF contrast along the growth axis with an "anti-symmetric" distribution with respect to the axis of the InGaN NN. Also, because of the thickest integration around the axis, a projected indium content maximum can be observed around this axis. Such results can be visualized by looking at a mechanical spring in a direction perpendicular to its axis. Spiral growth has been reported with the VLS growth mode in various materials [15-20]. Based on theories and simulations, its growth mechanism has been attributed to the formation of a screw dislocation in the early-stage of the growth [15,16,18,20]. The screw dislocation, which is expected to be easily formed in our InGaN growth, results in the helical deposition of an InGaN NN.

The alternating indium composition can be attributed to a non-critical super-saturation process during the VLS growth. In other words, there is a finite range of indium content for reaching the super-saturation and precipitation conditions in the Au droplet. From the overgrowth result of GaN (see Fig. 2), in which Au NPs are buried in GaN and no quasi-1-D structure is formed, it is reasonable to assume that Ga incorporation into the molten Au droplet is less effective than its direct deposition. Therefore, the grown indium composition is controlled by indium incorporation into the molten Au droplet at the needle top during the growth. During indium precipitations to form InGaN, the major part of Ga atoms is supplied directly from the vapor phase. Such a Ga atom supply is supposed to be quite stable. Once the super-saturation condition is reached, InGaN is deposited through precipitation

to form a high-indium layer of a couple nm in thickness. This super-saturation and hence precipitation condition can be maintained even though the indium content in the Au droplet is slightly reduced. Under such a condition, an InGaN layer of relatively lower indium content is grown until the next super-saturation stage is reached and another higher-indium InGaN layer is to be deposited. The mechanism for generating such a pulsed super-saturation process is still not known and deserves further investigation. It is noted that with the random distribution of Au NPs or InGaN NNs on the GaN template and the turbulent ambient vapor in the MOCVD growth chamber, the pulsed super-saturation process cannot follow a perfectly periodical pattern. Hence, the quasi-periodical behavior is observed.

5. Summary

In summary, the helical deposition of InGaN with a quasi-periodical indium content distribution along the growth direction for growing InGaN NNs with the VSL mode was observed based on the analyses of HAADF and EDX scanning measurement results along and perpendicular to the growth direction. The alternating indium content along the growth direction was attributed to a pulsed behavior of indium super-saturation process in the catalytic Au droplet at the top of an InGaN NN. The helical deposition could be due to the formation of screw-type dislocations around the bases of InGaN NNs for initiating spiral growth.

References:

1. L. W. Tu, C. L. Hsiao, T. W. Chi, I. Lo, and K. Y. Hsieh, Appl. Phys. Lett. **82**, 1601 (2003).
2. A. Kikuchi, M. Kawai, M. Tada, and K. Kishino, Jpn. J. Appl. Phys. **43**, L1524 (2004).
3. L. Cerutti, J. Ristiæ, S. Fernández-Garrido, E. Calleja, A. Trampert, K. H. Ploog, S. Lazic, and J. M. Calleja, Appl. Phys. Lett. **88**, 213114 (2006).
4. J. E. Van Nostrand, K. L. Averett, R. Cortez, J. Boeckl, C. E. Stutz, N. A. Sanford, A. V. Davydov, and J. D. Albrecht, J. Cryst. Growth **287**, 500 (2006).
5. S. D. Hersee, X. Sun, and X. Wang, Nano Lett. **6**, 1808 (2006).
6. Y. S. Chen, W. Y. Shiao, T. Y. Tang, W. M. Chang, C. H. Liao, C. H. Lin, K. C. Shen, C. C. Yang, M. C. Hsu, J. H. Yeh, and T. C. Hsu, J. Appl. Phys. **106**, 023521 (2009).
7. H. M. Kim, W. C. Lee, T. W. Kang, K. S. Chung, C. S. Yoon, and C. K. Kim, Chem. Phys. Lett. **380**, 181 (2003).
8. K. M. Wu, Y. Pan, and C. Liu, Appl. Sur. Sci. **255**, 6705 (2009).
9. R. S. Wagner and W. C. Ellis, Appl. Phys. Lett. **4**, 89 (1964).
10. J. V. Milewski, F. D. Gac, J. J. Petrovic, and S. R. Skaggs, J. Mater. Sci. **20**, 1160 (1985).
11. H. L. Qiu, C. B. Cao, X. Xiang, Y. H. Zhang, J. Li, and H. S. Zhu, J. Cryst. Growth **190**, 1 (2006).
12. T. Kuykendall, P. J. Pauzauskie, Y. F. Zhang, J. Goldberger, D. Sirbuly, J. Denlinger, and P. D. Yang, Nature Mater. **3**, 524 (2004).
13. T. Y. Tang, W. Y. Shiao, C. H. Lin, K. C. Shen, J. J. Huang, S. Y. Ting, T. C. Liu, C. C. Yang, C. L. Yao, J. H. Yeh, T. C. Hsu, W. C. Chen, and L. C. Chen, J. Appl. Phys. **105**, 023501 (2009).
14. C. Y. Chen, J. Y. Wang, F. J. Tsai, Y. C. Lu, Y. W. Kiang, and C. C. Yang, Opt. Express. **17**, 14186 (2009).
15. S. Harris and P. Smilauer, Phys. Rev. B **50**, 7952 (1994).
16. A. Karma and M. Plapp, Phys. Rev. Lett. **81**, 4444-4447 (1998).
17. A. Kimura, N. Futagawa, A. Usui, and M. Mizuta, J. Crystal Growth **229**, 53 (2001).
18. P. M. Martins and F. Rocha, Surface Science **601**, 3400-3408 (2007).
19. N. Wang, Y. Cai, and R. Q. Zhang, Materials Science and Engineering R **60**, 1-51 (2008).
20. A. Redinger, O. Ricken, P. Kuhn, A. Ra¨tz, A. Voigt, J. Krug, and T. Michely, Phys. Rev. Lett. **100**, 035506 (2008).

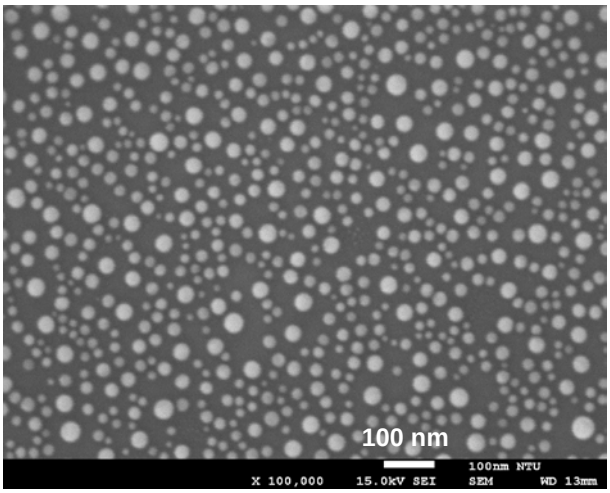

Fig. 1 A plan-view SEM image of Au NPs on a GaN template fabricated by laser irradiation.

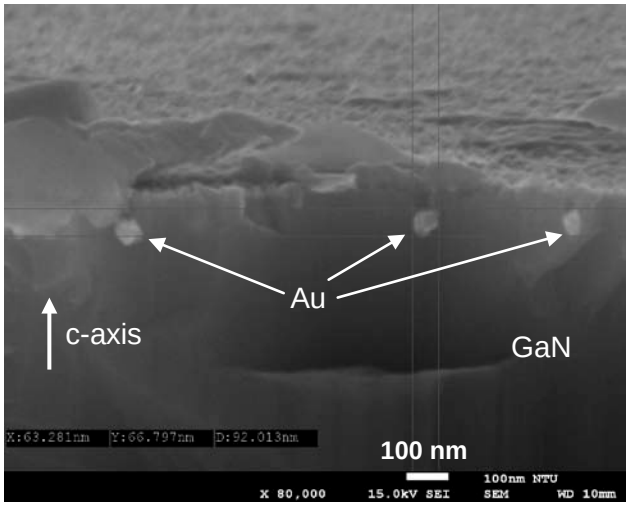

Fig. 2 A cross-section SEM image of a GaN layer with embedded Au NPs.

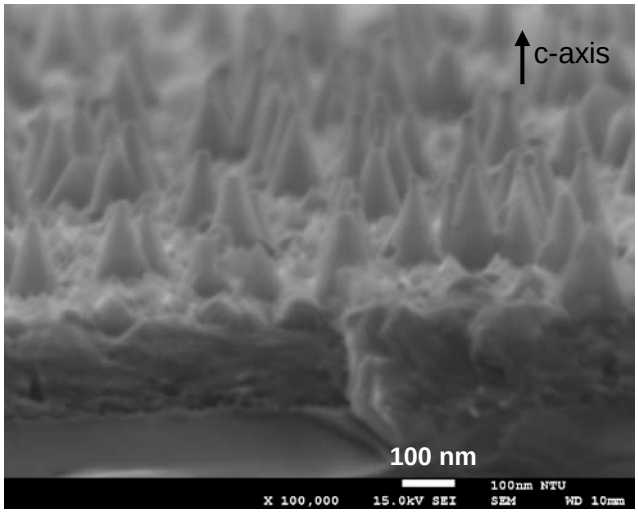

Fig. 3 A tilted SEM image of the grown InGaN NNs.

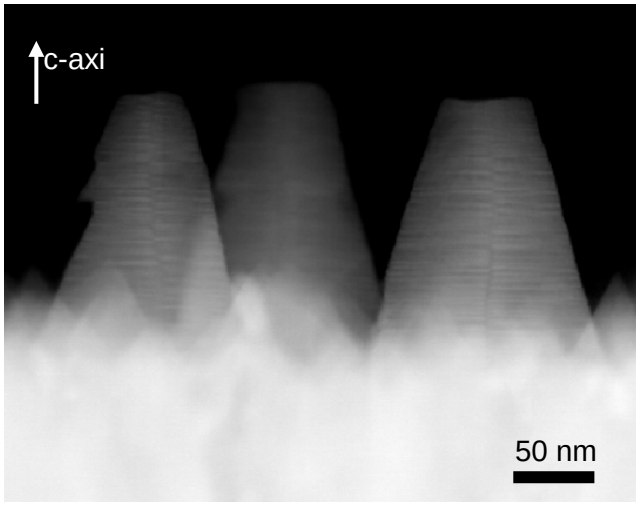

Fig. 4 A cross-section TEM HAADF image showing three InGaN NNs.

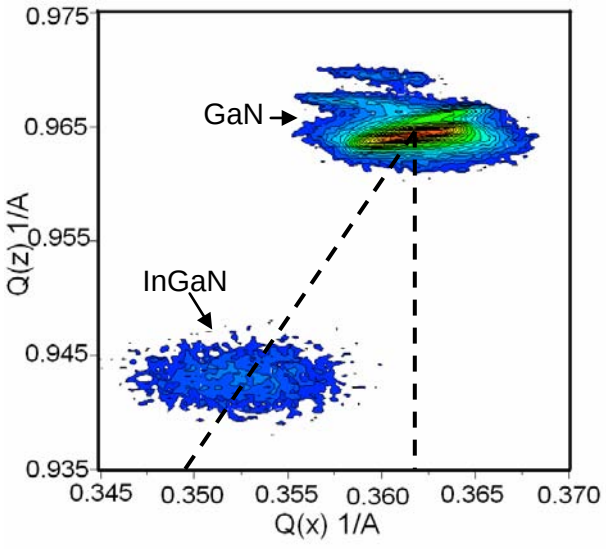

Fig. 5 RSM image of the InGaN NN sample with the vertical and slant dashed lines corresponding to the fully-strained and fully-strain-relaxed InGaN conditions, respectively.

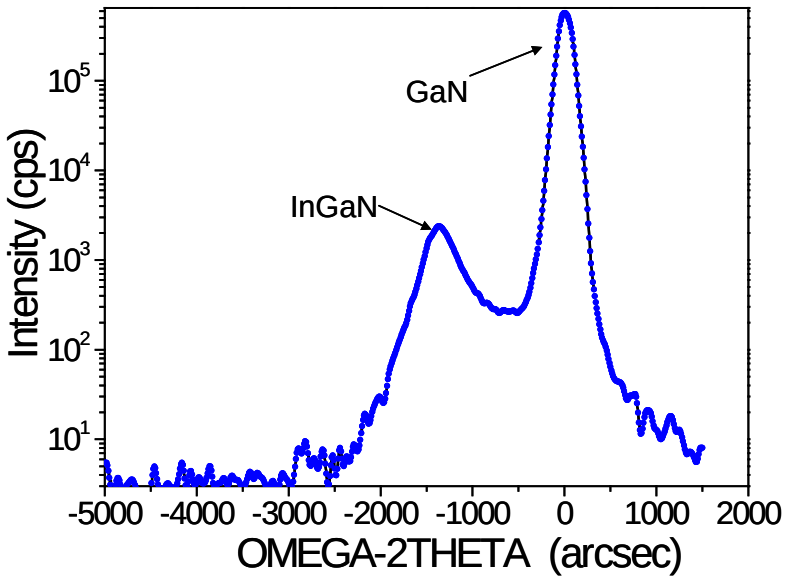

Fig. 6 XRD ω-2θ scan pattern of the InGaN NN sample.

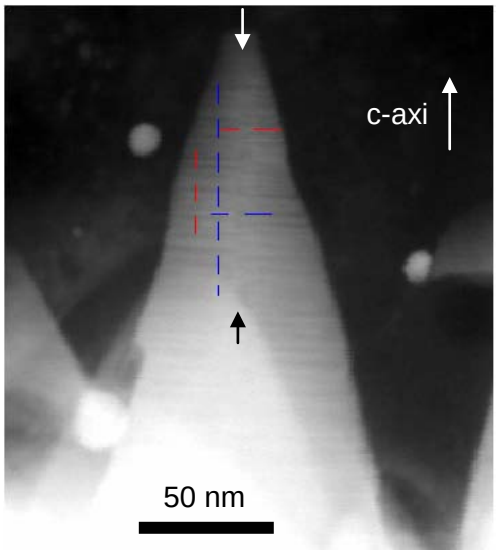

Fig. 7 HAADF close-up image of an InGaN NN. The vertical growth axis is indicated by the two short vertical arrows. Two horizontal and two vertical dashed lines are drawn to show the rough locations of HAADF and EDX scanning for analysis.

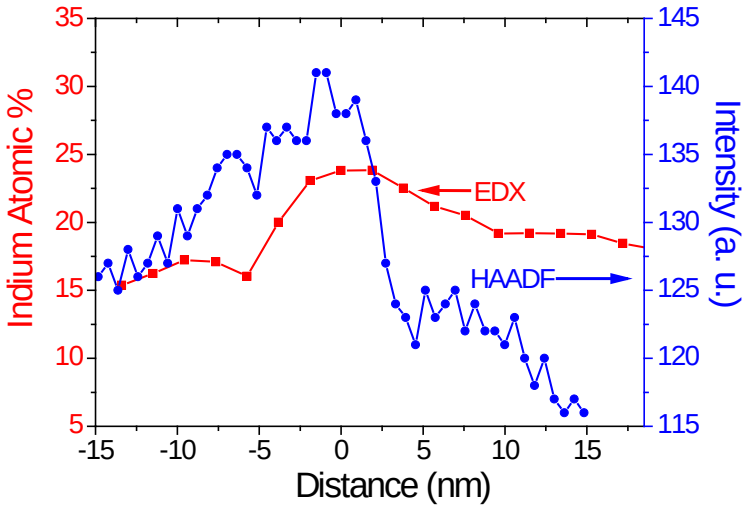

Fig. 8 Horizontal EDX (the left ordinate for indium atomic %) and HAADF (the right ordinate) data distributions along the horizontal dashed lines shown in Fig. 7.

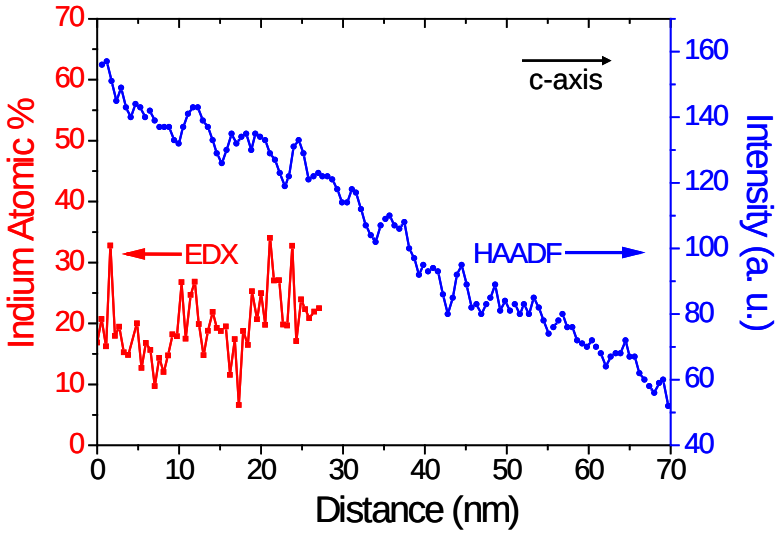

Fig. 9 Vertical EDX (the left ordinate for indium atomic %) and HAADF (the right ordinate) data distributions along the vertical dashed lines shown in Fig. 7.

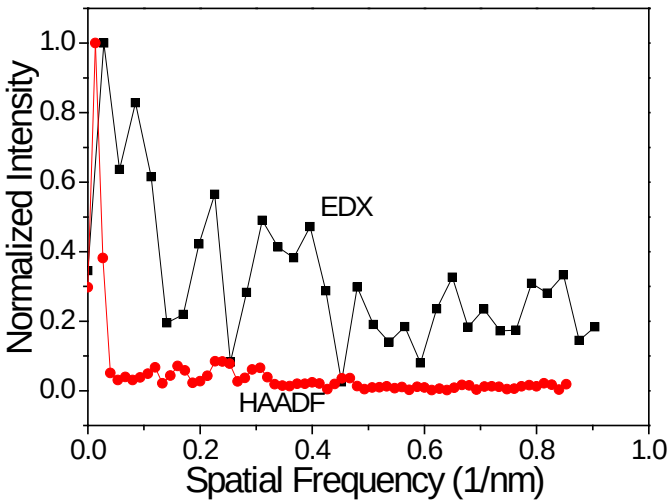

Fig. 10 Normalized spatial-frequency spectra of the HAADF and EDX data in Fig. 9.

List of Related Publications:

1. Wen-Ming Chang, Che-Hao Liao, Tsung-Yi Tang, Chih-Yen Chen, Yung-Sheng Chen, Wen-Yu Shiao, Yean-Woei Kiang, and C. C. Yang, "Helical deposition with alternating indium composition in growing an InGaN nano-needle with the vapor-liquid-solid growth mode," submitted to J. Crystal Growth.
2. Tsung-Yi Tang, Wen-Yu Shiao, Yung-Sheng Chen, Cheng-Hung Lin, Wen-Ming Chang, Che-Hao Liao, Kun-Ching Shen, C. C. Yang, Ming-Chi Hsu, Jui-Hung Yeh, and Ta-Cheng Hsu, "Nitride Nanocolumns for the Development of Light-emitting Diode," IEEE Transactions on Electron Devices, vol. 57, no. 1, pp. 71-78, January 2010. **(invited**)
3. G. Sun, J. B. Khurgin, and C. C. Yang, "Impact of High-Order Surface Plasmon Modes of Metal Nanoparticles on Enhancement of Optical Emission," Applied Physics Letters, Vol. 95, No. 17, p. 171103-1~3, 27 October 2009.
4. Cheng-Yen Chen, Jyh-Yang Wang, Fu-Ji Tsai, Yen-Cheng Lu, Yean-Woei Kiang, and C. C. Yang, "Fabrication of sphere-like Au nanoparticles on substrate with laser irradiation and their polarized localized surface plasmon behaviors," Optics Express, Vol. 17, No. 16, p. 14186~14198, 30 July 2009.